



## Correlation-enhanced Goos-Hänchen shift in Rydberg atomic gases

Di-Di Zheng, Hui-Min Zhao, Xiao-Jun Zhang <sup>\*</sup> and Jin-Hui Wu<sup>†</sup>

*School of Physics and Center for Quantum Sciences, Northeast Normal University, Changchun 130024, China*

 (Received 21 May 2022; revised 29 August 2022; accepted 13 October 2022; published 28 October 2022)

We present here a theoretical investigation on the Goos-Hänchen (GH) lateral shift of a probe field as it is reflected or transmitted from a three-layer system with a Rydberg atomic gas sandwiched between two dielectric slabs. Driven by this weak probe field and a strong-coupling field, Rydberg atoms with dipole-dipole interactions are capable of producing a nonlocal Kerr effect whose strength could far exceed the corresponding local Kerr effect at a rather low atomic density. The resultant GH shift is distinct from that observed in an extremely diluted atomic gas with negligible Rydberg-Rydberg interactions and has been examined in two particular cases specified by different coupling frequencies for a fixed probe frequency. In both cases, the nonlocal Kerr effect is found to result in an obvious enhancement of the GH shift and more importantly provide an alternative way for controlling the GH shift by varying the atomic density in an appropriate range. Finally, we present a possible realization of a highly sensitive displacement sensor by exploiting an approximately linear relation between the displacement of one dielectric slab and the GH shift of the probe field.

DOI: [10.1103/PhysRevA.106.043119](https://doi.org/10.1103/PhysRevA.106.043119)

### I. INTRODUCTION

A totally reflected light beam is well known to be laterally shifted from the position predicted by geometrical optics. This phenomenon typically referred to as the Goos-Hänchen (GH) shift is the result of a coherence or interference effect in wave optics [1,2]. The underlying physics lies in that the waves comprising an incident light beam acquire different phase changes in reflection owing to different wave vectors so that the reflected light beam must exhibit a lateral shift from the incident point since it cannot be perfectly reconstituted with these phase reformed waves [3,4]. This mechanism works also for partially reflected and transmitted light beams, which have been extensively studied in achieving and manipulating the GH shift [5–7] with the consideration that one usually has regular reflection but not total reflection.

As a generic phenomenon of wave mechanics, recently the GH shift was found to also exist in the reflections of spin waves [8], neutrons [9], electrons [10–12], etc. As far as the more familiar light beams are concerned, the GH shift has been investigated in various media and structures, such as dielectric slabs or laser dressed media [13–16], optical cavities or waveguides [17–20], photonic crystals [21], metasurfaces [22], optomechanical systems [23], and Weyl semimetals [24], showing diverse features of both fundamental and applied interests. One particular goal in these studies is to explore the promising potentials of developing new techniques for controlling the GH shift in order to build high-sensitivity sensors.

Typically, the linear optical responses of laser-dressed media [13,14,25] are utilized to observe and manipulate the GH shift. However, on the surfaces of various nonlinear me-

dia, e.g., that exhibit second-harmonic generation [26,27], Helmholtz solitons [28] and Airy beams [29], the GH shift holds more interesting physics and promises additional controls. The problem lies in that the nonlinear responses of most optical materials are too weak to be utilized. Far-off-resonance excitations are commonly used to evade large linear absorption but inevitably reduce the nonlinear interactions between atoms and photons. An effective scheme to attain both limited linear absorption and strong optical nonlinearity is electromagnetically induced transparency (EIT), with which the linear absorption at resonance is largely suppressed due to destructive interference between different transition pathways while the Kerr nonlinearity can be significantly enhanced because it is immune to this destructive interference [30–32].

On the other hand, recent theoretical and experimental investigations show that highly excited Rydberg atoms with large principal quantum numbers provide new opportunities to generate strong optical nonlinearities [33–35]. In short, large dipole moments of Rydberg states can give rise to strong dipole-dipole interactions between two atoms of distances up to several or more than ten microns, which then create effective atomic correlations viable to be mapped into nonlocal optical nonlinearities in the EIT regime [36–38]. The resultant nonlinear polarizations are many orders of magnitude larger than those obtained in the conventional EIT media and remain strong even at the single-photon level [39,40]. Rydberg states exhibit also long lifetimes up to hundreds of microseconds so that the induced optical nonlinearities are largely coherent during atom-light interactions [41,42].

We are then motivated to consider a three-layer system where a Rydberg atomic gas is sandwiched between two dielectric slabs as shown in Fig. 1 by aiming at the GH shift of a probe field in regular reflection and transmission. This Rydberg atomic gas dressed by the probe field and another coupling field in the EIT regime is found to exhibit

<sup>\*</sup>zhangxj037@nenu.edu.cn

<sup>†</sup>jhwu@nenu.edu.cn

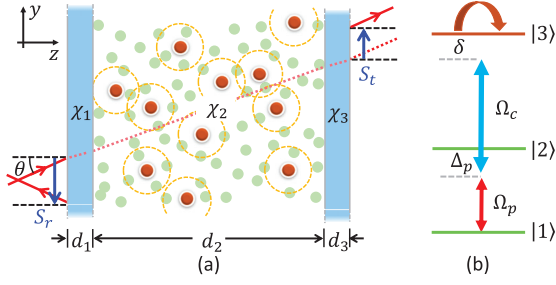


FIG. 1. (a) Schematic of a three-layer system formed by two dielectric slabs with susceptibilities  $\chi_1$  and  $\chi_3$  and a sandwiched atomic gas with susceptibility  $\chi_2$ . (b) A ladder configuration with the three levels assumed, e.g., to be  $|1\rangle = |5S_{1/2}, F = 2\rangle$ ,  $|2\rangle = |5P_{3/2}, F = 3\rangle$ , and  $|3\rangle = |60S_{1/2}\rangle$  for  $^{87}\text{Rb}$  atoms driven by a probe ( $\Omega_p$ ) and a coupling ( $\Omega_c$ ) field. An example of the negative (positive) lateral shift is shown for a reflected (transmitted) component of the probe field incident from the left dielectric slab. Each orange-dashed circle refers to a blockade sphere, in which one atom in the Rydberg state  $|3\rangle$  denoted by a dark red dot forbids other atoms denoted by the light green dots to be excited via dipole-dipole interactions.

a significant nonlocal Kerr effect arising from dipole-dipole interactions, in addition to a weak local Kerr effect and a comparable local linear response. Taking the respective susceptibilities into a transfer matrix, it is viable to further examine the GH shift of a partially reflected or transmitted probe field in a wide range of the incident angle. We focus on two cases where the local linear susceptibility (i) vanishes in its real part so that the probe reflection is essentially determined by the nonlocal nonlinear susceptibility or (ii) is well counteracted by the nonlocal nonlinear susceptibility in its imaginary part to cause a great suppression of the probe absorption. In both cases, the GH shift is greatly enhanced as compared with that attained in the absence of Rydberg-Rydberg interactions. Another intriguing feature is that the GH shift depends critically on the atomic density in the sense that a slight increase of the atomic density results in a dramatic enhancement of the GH shift. This feature is promising for realizing a sensitive displacement sensor because the maximal GH shift moves evidently to another incident angle as one dielectric slab suffers a tiny displacement for a proper atomic density.

The organization of this article is as follows: In Sec. II, we introduce the model and relevant equations for examining the GH shift in reflection and transmission. The emphasis will be placed on how to derive the linear and nonlinear susceptibilities of sandwiched Rydberg atoms. Section III shows numerical results and relevant discussions on the GH shift enhanced by the nonlocal Kerr susceptibility in two specific cases. The second case is further explored for realizing a displacement sensor with respect to one dielectric slab. Finally, we draw our conclusions in Sec. IV, while detailed equations for deriving the nonlocal Kerr susceptibility are given in the Appendix.

## II. MODEL AND EQUATIONS

We consider a transverse-electric (TE) polarized laser beam acting as a probe field that is incident upon a cavity from

vacuum and then gets divided into the reflected and transmitted beams, as shown by the solid-line arrows in Fig. 1(a). The cavity is composed of three layers of homogeneous media: two parallel dielectric slabs with susceptibilities  $\chi_1$  and  $\chi_3$  and thicknesses  $d_1$  and  $d_3$  separated by an atomic gas with susceptibility  $\chi_2$  and thickness  $d_2$ . The reflectivities of both dielectric slabs are not too high in the absence of high-reflecting coatings on their surfaces so that the three-layer system should not be considered as a high-quality cavity with an extremely-frequency-sensitive response, hence allowing the probe field to come in and be partially reflected and transmitted. On the surface of the left (right) slab, a lateral shift may exist between the center point of the reflected (transmitted) beam and the corresponding point predicted by geometrical optics [see the red dotted line in Fig. 1(a)]. Based on the stationary phase theory [3,4,43], the lateral shifts of reflected and transmitted beams can be calculated via

$$S_r = -\frac{c}{\omega_p \cos \theta} \frac{\partial \phi_r}{\partial \theta},$$

$$S_t = -\frac{c}{\omega_p \cos \theta} \frac{\partial \phi_t}{\partial \theta}, \quad (1)$$

where  $\theta$  ( $\omega_p$ ) is the incident angle (angular frequency) of the probe field, while  $\phi_r$  ( $\phi_t$ ) is the phase of the reflection  $r$  (transmission  $t$ ) coefficient. Note that a positive  $S_t$  and a negative  $S_r$  have been shown in Fig. 1(a) when they are, respectively, in the same and opposite directions of the  $y$  component of the probe wave vector. It is also worth noting that a detailed derivation of Eq. (1) as in Ref. [4] indicates that  $S_r$  and  $S_t$  actually result from the interference between plane waves of different momentums (wave vectors) parallel to the cavity surface.

Now we briefly explain how to calculate  $r$  and  $t$  via the standard transfer-matrix approach [44]. For a weak probe field passing through the  $j$ th layer with  $j \in \{1, 2, 3\}$ , the corresponding transfer matrix can be written as

$$M_j = \begin{bmatrix} \cos(k_z^j d_j) & i \sin(k_z^j d_j)/q_j \\ iq_j \sin(k_z^j d_j) & \cos(k_z^j d_j) \end{bmatrix}, \quad (2)$$

where  $k_z^j = k_p(\epsilon_j - \sin^2 \theta)^{1/2}$  is the  $z$  component of the probe wave vector in the  $j$ th layer with  $\epsilon_j = 1 + \chi_j$ ,  $k_p = \omega_p/c$ , and  $q_j = k_z^j/k_p$ . Then we have the total transfer matrix  $M = M_1 M_2 M_3$  for the considered cavity as a product of those for different layers. With the diagonal and off-diagonal elements of matrix  $M$ , we further have the reflection and transition coefficients

$$r = \frac{q_0(M_{22} - M_{11}) - (q_0^2 M_{12} - M_{21})}{q_0(M_{22} + M_{11}) - (q_0^2 M_{12} + M_{21})}, \quad (3a)$$

$$t = \frac{2q_0}{q_0(M_{22} + M_{11}) - (q_0^2 M_{12} + M_{21})}, \quad (3b)$$

with  $q_0 = \cos \theta$ . Substituting the phases of  $r = |r|e^{i\phi_r}$  and  $t = |t|e^{i\phi_t}$  into Eq. (1), it is straightforward to calculate the lateral shifts of both reflected and transmitted probe beams. Above discussions clearly show that  $S_r$  and  $S_t$  depend on the incident angle  $\theta$  and the angular frequency  $\omega_p$  of the probe field as well as the thicknesses  $d_1$ ,  $d_2$ , and  $d_3$  and the susceptibilities  $\chi_1$ ,  $\chi_2$ , and  $\chi_3$  of different layers.

It is of particular interest that  $\chi_2$  describes the optical response of a sandwiched atomic gas to the weak probe field and offers us a flexible avenue to control  $S_r$  and  $S_t$  since  $\chi_2$  can be modified on demand by another strong-coupling field. Specifically, this atomic gas is assumed to be driven into a three-level ladder-type EIT configuration as shown in Fig. 1(b). The refracted probe field (after passing the left slab and before leaving from the right slab) interacts with different atoms by driving the  $|1\rangle \leftrightarrow |2\rangle$  transition of resonant frequency  $\omega_{21}$  at a single-photon detuning  $\Delta_p = \omega_{21} - \omega_p$ . Meanwhile, the coupling field of angular frequency  $\omega_c$  (traveling, e.g., along the  $y$  direction) drives the  $|2\rangle \leftrightarrow |3\rangle$  transition of resonant frequency  $\omega_{32}$  at a single-photon detuning  $\Delta_c = \omega_{32} - \omega_c$ . In this case, the optical response described by  $\chi_2$  depends critically on an important parameter: the double-photon detuning  $\delta$  defined as  $\delta = \Delta_c + \Delta_p = \omega_{31} - \omega_c - \omega_p$  that will be frequently used in the following discussions. In addition, we assume that level  $|3\rangle$  refers to a high Rydberg state with a long radiative lifetime, a large electric-dipole moment and a strong dipole-dipole interaction [45].

With above considerations, we can write down the total Hamiltonian for all coherently driven atoms [37]

$$\hat{H} = N_a \int d^3r \hat{H}(\mathbf{r}), \quad (4a)$$

as a volume integral of the local Hamiltonian  $\hat{H}(\mathbf{r})$  for a single atom at position  $\mathbf{r}$ . In this integral,  $N_a$  describes the atomic density while  $\hat{H}(\mathbf{r})$  is given by

$$\begin{aligned} \hat{H}(\mathbf{r})/\hbar = & \Delta_p \hat{S}_{22}(\mathbf{r}) + \delta \hat{S}_{33}(\mathbf{r}) \\ & - [\Omega_p \hat{S}_{12}(\mathbf{r}) + \Omega_c \hat{S}_{23}(\mathbf{r}) + \text{H.c.}] \\ & + N_a \int d^3r' \hat{S}_{33}(\mathbf{r}') V(\mathbf{r}' - \mathbf{r}) \hat{S}_{33}(\mathbf{r}), \end{aligned} \quad (4b)$$

with the single-atom transition ( $\alpha \neq \beta$ ) and projection ( $\alpha = \beta$ ) operators defined as  $\hat{S}_{\alpha\beta}(\mathbf{r}) = |\beta(\mathbf{r})\rangle\langle\alpha(\mathbf{r})|$  [38]. Here  $\Omega_p = \mu_{21}E_p/2\hbar$  and  $\Omega_c = \mu_{32}E_c/2\hbar$  are Rabi frequencies of the probe and coupling fields of amplitudes  $E_p$  and  $E_c$ , respectively, with  $\mu_{21}$  and  $\mu_{32}$  being dipole matrix elements on the respective atomic transitions. We have also introduced the van der Waals (*vdW*) potential  $V(\mathbf{r} - \mathbf{r}') = C_6/|\mathbf{r} - \mathbf{r}'|^6$  [46] with  $C_6 = 2\pi \times 140 \text{ GHz } \mu\text{m}^6$  for the  $|3\rangle = |60S_{1/2}\rangle$  state of  $^{87}\text{Rb}$  atoms to model the Rydberg-Rydberg interaction between one atom at position  $\mathbf{r}$  and another atom at position  $\mathbf{r}'$ . Then the integral describes that the atom at a fixed position  $\mathbf{r}$  exhibits an energy shift in state  $|3\rangle$  as induced by its nonlocal interactions with other atoms at variable positions  $\mathbf{r}'$ .

The optical response of an atom at position  $\mathbf{r}$  to the probe field is determined by  $\rho_{21}(\mathbf{r})$  defined as the expectation value  $\langle \hat{S}_{21}(\mathbf{r}) \rangle$ . It is indeed a one-body density-matrix element and can be calculated via the optical Bloch equation  $i\hbar\partial_t \langle \hat{S}_{\alpha\beta}(\mathbf{r}) \rangle = \langle [\hat{S}_{\alpha\beta}(\mathbf{r}), \hat{H}(\mathbf{r})] \rangle$  as

$$\begin{aligned} \partial_t \rho_{21}(\mathbf{r}) = & -g_{21}\rho_{21}(\mathbf{r}) + i\Omega_c^* \rho_{31}(\mathbf{r}) \\ & + i\Omega_p [\rho_{11}(\mathbf{r}) - \rho_{22}(\mathbf{r})], \end{aligned} \quad (5a)$$

with  $g_{21} = \gamma_{21} + i\Delta_p$  and  $\gamma_{21}$  denoting the decoherence rate of  $\rho_{21}(\mathbf{r})$ . As we can see, this equation further relates to

$\rho_{31}(\mathbf{r})$ , whose dynamic evolution is governed by

$$\begin{aligned} \partial_t \rho_{31}(\mathbf{r}) = & -g_{31}\rho_{31}(\mathbf{r}) + i\Omega_c \rho_{21}(\mathbf{r}) - i\Omega_p \rho_{32}(\mathbf{r}) \\ & - iN_a \int d^3r' V(\mathbf{r}' - \mathbf{r}) \rho_{33,31}(\mathbf{r}', \mathbf{r}), \end{aligned} \quad (5b)$$

with  $g_{31} = \gamma_{31} + i\delta$  and  $\gamma_{31}$  denoting the decoherence rate of  $\rho_{31}(\mathbf{r})$ . The other one-body dynamic equations are listed in the Appendix and can be solved together with Eqs. (5a) and (5b) to calculate  $\rho_{21}(\mathbf{r})$  in the steady state, provided the two-body density matrix elements  $\rho_{33,31}(\mathbf{r}', \mathbf{r})$  are known. Here  $\rho_{\alpha\beta,\mu\nu}(\mathbf{r}', \mathbf{r})$  is defined as  $\langle \hat{S}_{\alpha\beta}(\mathbf{r}') \hat{S}_{\mu\nu}(\mathbf{r}) \rangle$  and represents the quantum correlation between two atoms at positions  $\mathbf{r}'$  and  $\mathbf{r}$ , respectively. The calculation of  $\rho_{33,31}(\mathbf{r}', \mathbf{r})$  in the steady state involves another set of two-body dynamic equations, which can be attained from the set of one-body dynamic equations via  $\partial_t \langle \hat{S}_{\alpha\beta}(\mathbf{r}') \hat{S}_{\mu\nu}(\mathbf{r}) \rangle = \langle \partial_t \hat{S}_{\alpha\beta}(\mathbf{r}') \hat{S}_{\mu\nu}(\mathbf{r}) \rangle + \langle \hat{S}_{\alpha\beta}(\mathbf{r}') \partial_t \hat{S}_{\mu\nu}(\mathbf{r}) \rangle$ . Taking  $\rho_{33,31}(\mathbf{r}', \mathbf{r})$  as an example, its dynamic evolution is found to obey

$$\begin{aligned} \partial_t \rho_{33,31}(\mathbf{r}', \mathbf{r}) = & -[g_{33,31} + iV(\mathbf{r}' - \mathbf{r})] \rho_{33,31}(\mathbf{r}', \mathbf{r}) \\ & + i\Omega_c [\rho_{33,21}(\mathbf{r}', \mathbf{r}) + \rho_{31,23}(\mathbf{r}', \mathbf{r})] \\ & - i\Omega_c^* \rho_{32,31}(\mathbf{r}', \mathbf{r}) - i\Omega_p \rho_{33,32}(\mathbf{r}', \mathbf{r}) \\ & - iN_a \int d^3r'' V(\mathbf{r}'' - \mathbf{r}) \rho_{33,33,31}(\mathbf{r}'', \mathbf{r}', \mathbf{r}), \end{aligned} \quad (6)$$

with  $g_{33,31} = g_{31} + \Gamma_{32}$  and  $\Gamma_{32}$  denoting the population decay rate of  $\rho_{33}(\mathbf{r}')$ . It is not of any surprise that Eq. (6) further involves a three-body density-matrix element  $\rho_{33,33,31}(\mathbf{r}'', \mathbf{r}', \mathbf{r}) = \langle \hat{S}_{33}(\mathbf{r}'') \hat{S}_{33}(\mathbf{r}') \hat{S}_{31}(\mathbf{r}) \rangle$  describing the quantum correlation between three atoms at positions  $\mathbf{r}''$ ,  $\mathbf{r}'$ , and  $\mathbf{r}$ , respectively. Note that the integration with respect to  $\mathbf{r}'$  and  $\mathbf{r}''$  in the above equations should be done under the requirement  $\mathbf{r}'' \neq \mathbf{r}' \neq \mathbf{r}$ . In the following, we just consider a few dilute-enough atomic media so that the contribution of three-body correlation  $\rho_{33,33,31}(\mathbf{r}'', \mathbf{r}', \mathbf{r})$  in Eq. (6) is negligibly small, as detailed in the last paragraph of this section.

The one-body and two-body dynamic equations are rather complicated and can be solved in the steady state by setting  $\partial_t \rho_{\alpha\beta}(\mathbf{r}) = \partial_t \rho_{\alpha\beta,\mu\nu}(\mathbf{r}', \mathbf{r}) = 0$  via the perturbation method with respect to a weak probe field. This perturbation method requires us to solve the  $n$ th-order components  $\rho_{\alpha\beta}^{(n)}(\mathbf{r})$  and  $\rho_{\alpha\beta,\mu\nu}^{(n)}(\mathbf{r}', \mathbf{r})$  order by order after making the series expansions  $\rho_{\alpha\beta}(\mathbf{r}) = \sum_{n=0}^{\infty} \rho_{\alpha\beta}^{(n)}(\mathbf{r})$  and  $\rho_{\alpha\beta,\mu\nu}(\mathbf{r}', \mathbf{r}) = \sum_{n=0}^{\infty} \rho_{\alpha\beta,\mu\nu}^{(n)}(\mathbf{r}', \mathbf{r})$ . To be more specific, we know that  $\rho_{\alpha\beta}^{(n)}(\mathbf{r})$  and  $\rho_{\alpha\beta,\mu\nu}^{(n)}(\mathbf{r}', \mathbf{r})$  are proportional to  $\Omega_p |\Omega_p|^{n-1}$  as  $n$  is an odd integer while to  $|\Omega_p|^n$  as  $n$  is an even integer. It is also known that some one-body density-matrix elements like  $\rho_{21}(\mathbf{r})$  have only the odd components  $\rho_{21}^{(n)}(\mathbf{r})$  with  $n \in \{1, 3, 5, \dots\}$  while others like  $\rho_{11}(\mathbf{r})$  have only the even components  $\rho_{11}^{(n)}(\mathbf{r})$  with  $n \in \{0, 2, 4, \dots\}$ . As for a two-body density-matrix element  $\rho_{\alpha\beta,\mu\nu}(\mathbf{r}', \mathbf{r})$ , its expansion is determined by those of two one-body counterparts  $\rho_{\alpha\beta}(\mathbf{r}')$  and  $\rho_{\mu\nu}(\mathbf{r})$ .

This perturbation method with more details shown in Ref. [37] has been used to attain the one-body first-order component  $\rho_{21}^{(1)}$ , which is irrelevant to Rydberg-Rydberg interactions and hence independent of position  $\mathbf{r}$ . Then we can

write down the linear susceptibility

$$\chi_2^{(1)} = \frac{N_a \mu_{21}^2}{\epsilon_0 \hbar} \frac{\rho_{21}^{(1)}}{\Omega_p} = \frac{N_a \mu_{21}^2}{\epsilon_0 \hbar} \frac{ig_{31}}{g_{21}g_{31} + |\Omega_c|^2}, \quad (7)$$

describing the linear optical response of a typical three-level EIT system. With the same method, we have also attained the one-body third-order component

$$\begin{aligned} \rho_{21}^{(3)} = & \frac{\Omega_p [2ig_{31}\rho_{11}^{(2)} + ig_{31}\rho_{33}^{(2)} + \Omega_c^* \rho_{32}^{(2)}]}{g_{21}g_{31} + |\Omega_c|^2} \\ & + \frac{\Omega_c^*}{g_{21}g_{31} + |\Omega_c|^2} N_a \int d^3r' V(\mathbf{r}' - \mathbf{r}) \rho_{33,31}^{(3)}(\mathbf{r}', \mathbf{r}), \end{aligned} \quad (8)$$

where the one-body second-order components  $\rho_{11}^{(2)}$ ,  $\rho_{33}^{(2)}$ , and  $\rho_{32}^{(2)}$  are irrelevant to Rydberg-Rydberg interactions again and hence position independent. In a thick-enough atomic gas, it is viable to further consider that the position dependence of the two-body third-order component  $\rho_{33,31}^{(3)}(\mathbf{r}', \mathbf{r})$  can be averaged out by the volume integral because  $V(\mathbf{r}' - \mathbf{r})$  reduces rapidly with the increase of  $|\mathbf{r}' - \mathbf{r}|$  so that it is safe to neglect the boundary effect for most interacting atoms. It is why  $\rho_{21}^{(3)}$  has been rewritten in a position-independent form, with which we can write down the following Kerr nonlinear susceptibility

$$\chi_2^{(3)} = \chi_a^{(3)} + \chi_R^{(3)} = \frac{N_a \mu_{21}^4}{4\epsilon_0 \hbar^3} \frac{\rho_{21}^{(3)}}{|\Omega_p|^2 \Omega_p}, \quad (9)$$

divided into a local ( $\chi_a^{(3)}$ ) and a nonlocal ( $\chi_R^{(3)}$ ) component. Here  $\chi_a^{(3)}$  refers to the first term on the right-hand side of Eq. (8) and can be realized even with independent atoms in the absence of Rydberg-Rydberg interactions, while  $\chi_R^{(3)}$  refers to the second term on the right-hand side of Eq. (8) and can be realized only with correlated atoms exhibiting Rydberg-Rydberg interactions.

The local nonlinear susceptibility takes the form

$$\begin{aligned} \chi_a^{(3)} = & \frac{N_a \mu_{21}^4}{4\epsilon_0 \hbar^3} \left\{ \frac{2ig_{31}}{\mathcal{P}_1} \left( -\frac{g_{31}}{\Gamma_{21}\mathcal{P}_1} - \frac{|\Omega_c|^2 g_{23}}{\mathcal{P}_1 \mathcal{P}_2} + \text{c.c.} \right) \right. \\ & + \frac{ig_{31}|\Omega_c|^2}{\mathcal{P}_1} \left( \frac{2\gamma_{32}g_{31} + \Gamma_{21}g_{32}}{\Gamma_{21}\mathcal{P}_1\mathcal{P}_2} + \text{c.c.} \right) \\ & + \frac{|\Omega_c|^2}{\Gamma_{21}\mathcal{P}_1\mathcal{P}_2} \left[ \frac{ig_{23}\Gamma_{32}\Gamma_{21}}{\mathcal{P}_1^*} + \left( \frac{ig_{23}\Gamma_{32}g_{31}}{\mathcal{P}_1^*} + \text{c.c.} \right) \right. \\ & \left. \left. + \left( \frac{i\Gamma_{21}|\Omega_c|^2}{\mathcal{P}_1^*} - \text{c.c.} \right) \right] \right\}, \end{aligned} \quad (10a)$$

with  $\mathcal{P}_1 = g_{21}g_{31} + |\Omega_c|^2$ ,  $\mathcal{P}_2 = \Gamma_{32}|g_{32}|^2 + 2\gamma_{32}|\Omega_c|^2$ , and  $g_{32} = g_{23}^* = \gamma_{32} + i\Delta_c$ . Here we have also introduced  $\gamma_{32}$  to denote the decoherence rate of  $\rho_{32}(\mathbf{r})$  and  $\Gamma_{21}$  to denote the population decay rate of  $\rho_{22}(\mathbf{r})$ . The nonlocal nonlinear susceptibility takes the form

$$\chi_R^{(3)} = \frac{N_a^2 \mu_{21}^4}{4\epsilon_0 \hbar^3} \frac{\Omega_c^*}{\mathcal{P}_1} \int d^3r' V(\mathbf{r}' - \mathbf{r}) \frac{\rho_{33,31}^{(3)}(\mathbf{r}', \mathbf{r})}{|\Omega_p|^2 \Omega_p}, \quad (10b)$$

and will be solved numerically together with Eq. (A2) in the Appendix since it is difficult or impossible to attain the analytical solution of  $\rho_{33,31}^{(3)}(\mathbf{r}', \mathbf{r})$ . Equation (10b) indicates that the two-body correlation between an atom at position  $\mathbf{r}'$

characterized by  $\rho_{33}^{(2)}$  and another atom at position  $\mathbf{r}$  characterized by  $\rho_{31}^{(1)}$  may largely alter the optical response to the probe field  $\Omega_p$  with the help of the coupling field  $\Omega_c$  and the  $vdW$  potential  $V(\mathbf{r}' - \mathbf{r})$ .

Up to the third-order expansion, the total optical response of the atomic gas to the probe field is

$$\chi_2 = \chi_2^{(1)} + \chi_a^{(3)} |E_p|^2 + \chi_R^{(3)} |E_p|^2, \quad (11)$$

which will be examined via numerical calculations in the regime of  $\Delta_p \gg \gamma_{21}$  to avoid significant probe absorption due to the single-photon excitation of intermediate state  $|2\rangle$  [38]. In this regime, we can determine the radius of a blockade sphere  $R_b = (|C_6 \Delta_p| / |\Omega_c|^2)^{1/6}$  [41,46], a distance from one Rydberg atom within which other atoms hardly get excited to the Rydberg state  $|3\rangle$  [47] owing to large energy shifts caused by Rydberg-Rydberg interactions. In this regard, the volume integral in Eq. (10b) needs to be performed from  $|\mathbf{r}' - \mathbf{r}| = R_b$  to  $|\mathbf{r}' - \mathbf{r}| = \infty$ , with the upper limit  $\infty$  referring in fact to a finite value roughly less than  $3R_b$  because  $V(\mathbf{r}' - \mathbf{r})$  rapidly reduces to become vanishing with the increase of  $|\mathbf{r}' - \mathbf{r}|$ .

In Fig. 2, we examine the total optical response  $\chi_2$  to the probe field as well as its three linear and nonlinear components against the double-photon detuning  $\delta$  with a probe detuning fixed as  $\Delta_p/2\pi = -160$  MHz and a coupling detuning tuned around  $\Delta_c = -\Delta_p$ . Figure 2(a) shows that the coupling field shifts the resonant frequency of the linear susceptibility  $\chi_2^{(1)}$  (i.e., that of the Rydberg state  $|3\rangle$ ) by an amount  $-|\Omega_c|^2/\Delta_c \approx -2.13\gamma_{21}$ . It is also clear that the linear absorption characterized by  $\text{Im}\chi_2^{(1)} > 0$  appears quite weak because the probe field is far detuned from transition  $|1\rangle \leftrightarrow |2\rangle$ . Figures 2(b) and 2(c) show that the local ( $\chi_a^{(3)} |E_p|^2$ ) and nonlocal ( $\chi_R^{(3)} |E_p|^2$ ) nonlinear responses exhibit resonant features near  $\delta \approx -2.13\gamma_{21}$  as well, although the former is much weaker than the latter. Hence, the total probe response  $\chi_2$  shown in Fig. 2(d) is mainly determined by the comparable linear ( $\chi_2^{(1)}$ ) and nonlocal nonlinear ( $\chi_R^{(3)} |E_p|^2$ ) responses.

It is worth noting that the nonlocal nonlinear response could (i) be made even stronger than the linear response by increasing  $\Omega_p$  because the former is proportional to  $|\Omega_p|^2$  while the latter is independent of  $\Omega_p$  [cf. Eq. (11)]; (ii) exhibit a quicker rise than the linear and local nonlinear responses as  $N_a$  increases because  $\chi_R^{(3)}$  is proportional to  $N_a^2$  while  $\chi_a^{(3)}$  and  $\chi_2^{(1)}$  are both proportional to  $N_a$  [cf. Eqs. (7), (10a), and (10b)]. However, a few limitations have been imposed on the two quantities before Eq. (11) is finally attained. First of all, the probe field must be kept weak enough so as to ensure the perturbation method valid. Second, there should be no more than one Rydberg atom inside each blockade sphere, which requires  $\frac{4}{3}\pi R_b^3 N_a \rho_{33}^{(2)} \leq 1$  with  $\rho_{33}^{(2)} \propto |\Omega_p|^2$  being the lowest-order nonzero component of Rydberg population  $\rho_{33}$ . Finally, three-body correlations should be negligible when calculating  $\rho_{33,31}(\mathbf{r}', \mathbf{r})$  in Eq. (6), which requires  $1 < \frac{4}{3}\pi (3R_b)^3 N_a \rho_{33}^{(2)} < 2$ . This requirement indicates that there exist less than two, but more than one, Rydberg atoms outside a blockade sphere of radius  $R_b$  and meanwhile inside a concentric sphere of radius  $3R_b$ . These limitations can be simultaneously satisfied in the case of  $N_a < 5 \times 10^{10} \text{ cm}^{-3}$  and  $\Omega_p = 0.01\gamma_{21}$  with  $R_b \simeq 5 \mu\text{m}$  attained for the parameters used in Fig. 2.

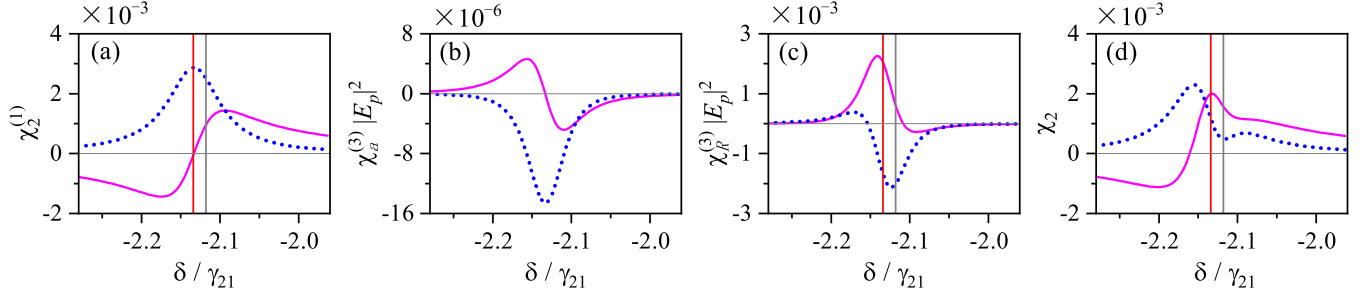


FIG. 2. (a) Linear  $\chi_2^{(1)}$ , (b) local nonlinear  $\chi_a^{(3)}|E_p|^2$ , and (c) nonlocal nonlinear  $\chi_R^{(3)}|E_p|^2$  susceptibilities as well as the (d) total probe susceptibility  $\chi_2$  plotted as a function of the double-photon detuning  $\delta/\gamma_{21}$ . These susceptibilities are shown as pink-solid lines for their real parts and as blue-dashed lines for their imaginary parts. The vertical red and gray lines refer, respectively, to  $\delta = -2.13\gamma_{21}$  and  $\delta = -2.12\gamma_{21}$  as two cases of special interest. Other parameters used in calculations are  $\Gamma_{21}/2\pi = 6$  MHz,  $\Gamma_{32}/2\pi = 3$  kHz,  $\gamma_{32} \approx \gamma_{21} \approx \Gamma_{21}/2$ ,  $\gamma_{31} \approx \Gamma_{31}/2$ ,  $\Delta_p/2\pi = -160$  MHz,  $\Omega_c/2\pi = 32$  MHz,  $\Omega_p = 0.01\gamma_{21}$  equivalent to  $E_p = 1.11$  V m $^{-1}$ ,  $\lambda_p = 780$  nm,  $\mu_{21} = 3.58 \times 10^{-29}$  C m, and  $N_a = 4.0 \times 10^{10}$  cm $^{-3}$ .

### III. THE LATERAL SHIFT

In this section, we focus on typical characteristics of the lateral shifts of both reflected and transmitted probe fields by paying attention to the important roles of the nonlocal Kerr nonlinearity. It is of particular interest to note from Fig. 2 that, in a narrow range of  $\delta$ ,  $\text{Im}\chi_2^{(1)}$  and  $\text{Im}\chi_R^{(3)}|E_p|^2$  have the opposite signs so as to yield a reduced absorption coefficient while  $\text{Re}\chi_2^{(1)}$  and  $\text{Re}\chi_R^{(3)}|E_p|^2$  have an identical sign so as to yield an enhanced refractive index. These features, desired for attaining large lateral shifts, inspire us to consider two specific cases: (I)  $\delta \simeq -2.13\gamma_{21}$  marked by the vertical red lines, at which  $\text{Re}\chi_2^{(1)}$  vanishes as shown in Fig. 2(a) and  $\text{Re}\chi_2$  is mainly determined by  $\text{Re}\chi_R^{(3)}$ ; (II)  $\delta \simeq -2.12\gamma_{21}$  marked by the vertical gray lines, at which  $\text{Im}\chi_R^{(3)}$  well counteracts  $\text{Im}\chi_2^{(1)}$  and a dip appears in  $\text{Im}\chi_2$  as shown in Fig. 2(d). Note that  $\text{Im}\chi_a^{(3)} < 0$  in Fig. 2(b) and  $\text{Im}\chi_R^{(3)} < 0$  in Fig. 2(c) do not mean an amplification of the probe field because the overall probe response is determined by  $\chi_2$  and the atomic medium exhibits loss (gain) only if  $\text{Im}\chi_2$  is positive (negative). We further assume  $d_1 = d_3 = 5$   $\mu\text{m}$  and  $\chi_1 = \chi_3 = 1.22$  for the two dielectric slabs. Then it is viable to calculate the lateral shifts of reflected and transmitted probe fields via Eqs. (3a) and (3b) after taking  $d_2 = 95$   $\mu\text{m}$  and  $\chi_2$  in Fig. 2(d) into Eq. (2).

The case I corresponding to  $\delta = -2.13\gamma_{21}$  is a situation where the probe and coupling fields are at exact resonance with the double-photon transition  $|1\rangle \leftrightarrow |3\rangle$ . The total probe susceptibility  $\chi_2 \simeq 0.002 + 0.001i$  attained in this case has been used to plot the reflection modulus  $|r|$ , the reflection phase  $\phi_r$ , and the lateral shift  $S_r$  as shown by the orange solid lines in Figs. 3(a1), 3(b1), and 3(c1). We find from Fig. 3(a1) that a series of minima in reflection modulus appear at certain incident angles, indicating cavity-like resonances between the incident probe field and the three-layer system. Each of these minimum is accompanied by a sharp change of reflection phase, as shown in Fig. 3(b1). Based on Eq. (1), we can say that such sharp phase changes will result in considerable lateral shifts of the reflected probe field, as shown in Fig. 3(c1). The largest lateral shift is seen to appear at  $\theta \simeq 0.14$  rad due to a sudden change of  $\phi_r$ , which is, however, meaningless as  $|r|$  is exactly vanishing.

To have an insight into the contribution of Rydberg-Rydberg interactions, we have presented relevant results attained in the absence of a nonlocal Kerr nonlinearity, i.e., with  $\chi_2 = \chi_2^{(1)} + \chi_a^{(3)}|E_p|^2 \simeq -5 \times 10^{-5} + 0.003i$ , as shown by the gray dashed lines in Figs. 3(a1), 3(b1), and 3(c1). A direct comparison of these orange solid and gray dashed lines shows that the lateral shift is evidently enhanced, when the nonlocal Kerr nonlinearity is included with  $\chi_R^{(3)} \neq 0$ , because the oscillations of  $|r|$  and  $\phi_r$  become more prominent. It is also important that larger lateral shifts can be achieved with stronger reflections as the incident angle increases. This is

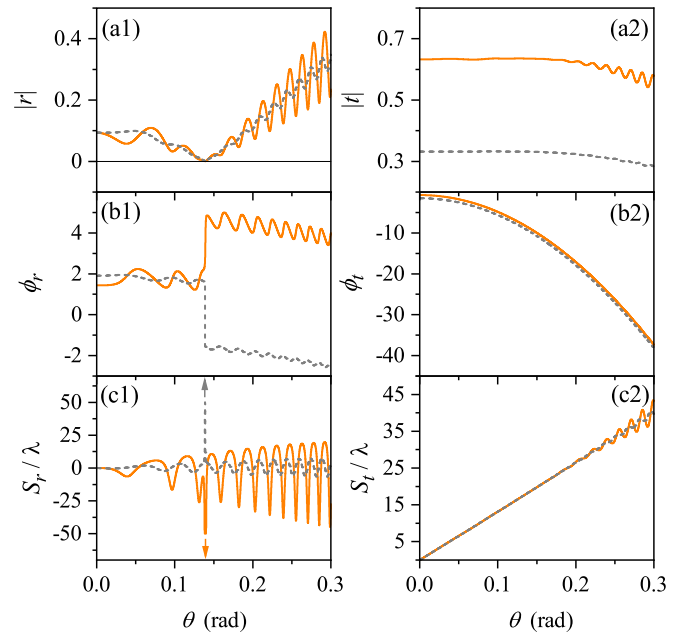


FIG. 3. (a1) Modulus  $|r|$  and (b1) phase  $\phi_r$  of the reflection coefficient as well as the corresponding (c1) lateral shift  $S_r$  are plotted with orange solid lines as a function of the incident angle  $\theta$ . For the transmitted field,  $|t|$ ,  $\phi_t$ , and  $S_t$  are plotted, respectively, in panels (a2), (b2), and (c2). The gray dashed lines describe relevant results attained in the absence of a nonlocal Kerr nonlinearity. Relevant parameters are the same as in Fig. 2 except  $\delta = -2.13\gamma_{21}$  corresponding to case I.

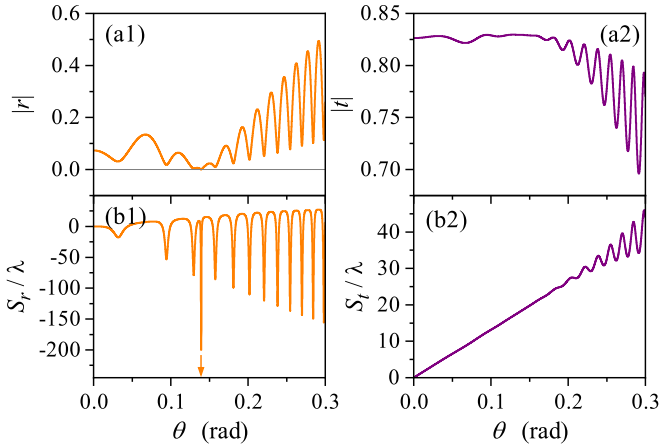


FIG. 4. (a1) Modulus  $|r|$  of the reflection coefficient and (b1) the corresponding lateral shift  $S_r$  against the incident angle  $\theta$ . For the transmitted field,  $|t|$  and  $S_t$  are plotted, respectively, in panels (a2) and (b2). Relevant parameters are the same as in Fig. 2 except  $\delta = -2.12\gamma_{21}$  corresponding to case II.

more or less contrary to the usual trade-off in the sense that the phase discontinuity on a lossless dielectric slab at resonance can give rise to a giant lateral shift with null reflection [13] while introducing weak absorption will yield minor but available reflection with an attenuated lateral shift [14,25]. It is thus clear that Rydberg-Rydberg interactions can reduce somewhat the trade-off between the lateral shift and the reflection modulus because  $\text{Re}\chi_R^{(3)}$  ( $\text{Im}\chi_R^{(3)}$ ) has a positive (negative) contribution to  $\text{Re}\chi_2$  ( $\text{Im}\chi_2$ ).

In Figs. 3(a2), 3(b2), and 3(c2), we plot modulus  $|t|$  and phase  $\phi_t$  of the transmission coefficient as well as the lateral shift  $S_t$  with the orange solid referring to  $\chi_R^{(3)} \neq 0$  while the gray dashed lines referring to  $\chi_R^{(3)} = 0$ . It is seen that the transmission modulus  $|t|$  can be greatly enhanced while the transmission phase  $\phi_t$  remains roughly unchanged as the nonlocal Kerr nonlinearity is included. In addition, the lateral shift seems independent of the nonlocal Kerr nonlinearity for smaller incident angles at which  $|t|$  and  $\phi_t$  always change smoothly with negligible oscillations. However, a difference occurs at the incident angles  $\theta > 0.2$  rad where  $|t|$  and  $\phi_t$  start to oscillate in the situation of  $\chi_R^{(3)} \neq 0$ , yielding thus slightly enhanced lateral shifts. It is of no doubt that greatly enhanced lateral shifts will be attained due to stronger oscillations of  $|t|$  and  $\phi_t$  at larger incident angles (not shown) as the nonlocal Kerr nonlinearity is included.

The case II corresponding to  $\delta \simeq -2.12\gamma_{21}$  is another intriguing situation where Rydberg-Rydberg interactions alter the optical response of the atomic gas mainly via the imaginary part of the nonlocal Kerr nonlinearity. In this case, we have indeed  $\chi_2 \simeq 0.002 + 5i \times 10^{-4}$  where the much smaller imaginary part indicates a minimum of the probe absorption due to the negative interplay of  $\text{Im}\chi_R^{(3)} < 0$  and  $\text{Im}\chi^{(1)} > 0$ . The further suppressed absorption then results in much larger lateral shifts, which is clear if we compare Fig. 4(b1) with Fig. 3(c1) to examine the lateral shift in reflection, and Fig. 4(b2) with Fig. 3(c2) to examine the lateral shift in transmission. It is also worth noting that the weaker prober absorption leads to stronger oscillations and larger magnitudes

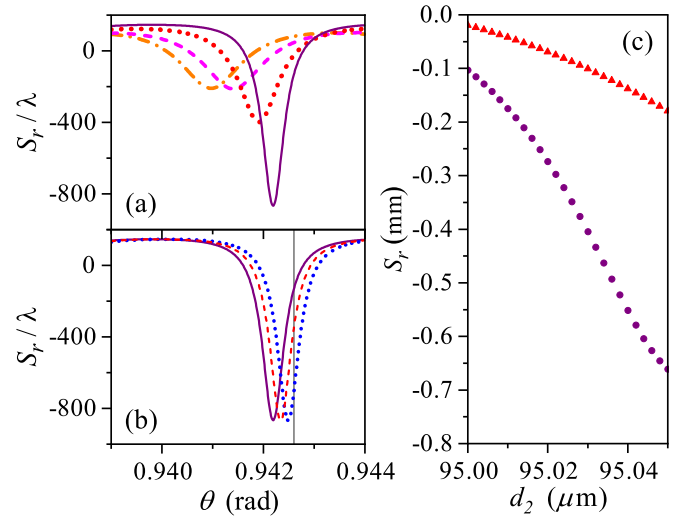


FIG. 5. (a) GH shift in reflection against incident angle for  $N_a = 2N_0$  (orange dash-dotted line),  $3N_0$  (pink dotted line),  $4N_0$  (red dashed line), and  $4.5N_0$  (purple solid line) plotted with  $d_2 = 95.00 \mu\text{m}$ . (b) GH shift in reflection against incident angle for  $d_2 = 95.00 \mu\text{m}$  (purple solid line),  $95.02 \mu\text{m}$  (red dashed line), and  $95.04 \mu\text{m}$  (blue dotted line) plotted with  $N_a = 4.5N_0$ . (c) GH shift in reflection against thickness of the atomic gas for  $N_a = 4N_0$  (red triangles) and  $4.5N_0$  (purple circles) plotted with  $\theta = 0.9426$  rad. Relevant parameters are the same as in Fig. 2 except  $N_0 = 1.0 \times 10^{10} \text{cm}^{-3}$  and  $\delta = -2.12\gamma_{21}$  corresponding to case II.

in reflection [Fig. 4(a1)] and transmission [Fig. 4(a2)], which hold promising potentials in the realization of highly sensitive sensors by exploiting relevant lateral shifts.

Applications of the enhanced lateral shifts have been explored, e.g., in measuring refractive index [48], displacement [49], temperature [50], relative humidity [51], and chemical vapors [52]. Taking the displacement sensor as an example, a slight variation of the medium thickness inside a cavity can lead to a dramatic adjustment of the lateral shifts in reflection and transmission [17,53,54]. To this end, we note that our Rydberg atomic gas has an amazing feature: Its optical response is more sensitive to the atomic density than other usual atomic gases because the nonlocal nonlinear susceptibility  $\chi_R^{(3)}$  is proportional to  $N_a^2$  but not  $N_a$  like the linear susceptibility  $\chi_2^{(1)}$  and the local nonlinear susceptibility  $\chi_a^{(3)}$ . That means, the contribution of two-body atomic correlations increases much faster than that of one-body atomic excitations as the mean interatomic distance becomes smaller. It is thus of interest to examine how the lateral shift  $S_r$  is controlled by the atomic density  $N_a$ .

In Fig. 5(a), we present the lateral shift  $S_r$  against incidence angle  $\theta$  in case II with different atomic densities. The results suggest that one  $S_r$  peak moves toward larger incident angles and meanwhile become higher in magnitude when the atomic density increases. The peak movement indicates a change of the corresponding resonance point determined by the real part of total susceptibility  $\chi_2$ , which can be enhanced by increasing the atomic density. The peak enhancement, however, should be a consequence of the suppressed absorption determined by the imaginary part of total susceptibility  $\chi_2$ , which can be reduced by increasing the atomic density. In particular, a

sharp and tall peak is observed at  $\theta \simeq 0.9422$  rad for  $N_a = 4.5 \times 10^{10} \text{ cm}^{-3}$ , which cannot be further increased so as to not break the validity of our perturbation calculations. This sharp and tall peak is an excellent candidate for exploring sensor applications, e.g., in the atomic layer thickness or the displacement of one dielectric slab. We then examine in Fig. 5(b) how it depends on the atomic thickness  $d_2$  by plotting  $S_r$  for  $d_2 = 95.00 \text{ }\mu\text{m}$ ,  $95.02 \text{ }\mu\text{m}$ , and  $95.04 \text{ }\mu\text{m}$ , respectively. It is found that the peak moves toward larger incident angles with negligible profile and magnitude changes as the atomic thickness  $d_2$  increases. More importantly, the three  $S_r$  peaks seem to be about equally spaced for the three  $d_2$  values of equal difference and a dramatic change of  $S_r$  seems to happen due to a tiny change of  $d_2$ , both of which are the desired effects for building a highly sensitive sensor.

In Fig. 5(c), we present the dependence of lateral shift  $S_r$  on atomic layer thickness  $d_2$  in a very small range of  $d_2 \in [95.00, 95.05] \text{ }\mu\text{m}$ . This is done for  $N_a = 4.0 \times 10^{10} \text{ cm}^{-3}$  and  $4.5 \times 10^{10} \text{ cm}^{-3}$ , which have been used to calculate the red dashed and purple solid lines, respectively, in Fig. 5(a). We have also chosen  $\theta = 0.9426$  rad as denoted by the vertical gray line in Fig. 5(b) where  $S_r$  is seen to increase with  $d_2$  for a fixed atomic density. From Fig. 5(c), we can see that an approximately linear relation holds between  $S_r$  and  $d_2$  for both curves denoted by red triangles and purple circles. Then a displacement sensor may be envisaged in case that a slight change of atomic layer thickness  $d_2$  is interpreted as a small displacement of one dielectric slab. It is clear that the slope of lateral shift against slab displacement depends on the atomic density, a steeper slope indicating a larger sensitivity is typically attained for a higher atomic density. We estimate, in particular, that the displacement sensitivity is approximately  $11.2 \text{ mm}/\mu\text{m}$  ( $3.2 \text{ mm}/\mu\text{m}$ ) for  $N_a = 4.5 \times 10^{10} \text{ cm}^{-3}$  ( $4.0 \times 10^{10} \text{ cm}^{-3}$ ).

#### IV. CONCLUSIONS

In summary, we have investigated the lateral GH shifts in both reflection and transmission for a probe field incident upon a three-layer system with a sandwiched Rydberg atomic gas. Numerical results show that Rydberg-Rydberg interactions can result in a remarkable nonlocal nonlinear response, which is much stronger than the local nonlinear response and meanwhile comparable to the linear response at a quite low atomic density. In two particular cases referring to different double-photon detunings, the nonlocal nonlinear response manifests itself in a maximum of the refractive index and a minimum of the absorption coefficient, respectively, in the total response as it is added to the linear response. This

then leads to sharp reflection and transmission resonances in both cases and hence enhanced lateral GH shifts at a series of incident angles of the probe field. The sensitivity of enhanced lateral GH shifts to density and thickness of the Rydberg atomic gas are then explored in case II to envisage a promising displacement sensor.

#### ACKNOWLEDGMENTS

This work is supported by the National Natural Science Foundation of China (No. 12074061), the National Key Research and Development Program of China (No. 2021YFE0193500), the Fundamental Research Funds for the Central Universities (No. 2412020FZ028), and the Scientific and Technological Research Program of Jilin Education Department (No. JJKH20211280KJ).

#### APPENDIX: ONE-BODY DENSITY-MATRIX EQUATIONS

In addition to Eqs. (5a) and (5b), other dynamic equations of one-body density-matrix elements are

$$\frac{\partial}{\partial t} \rho_{11} = \Gamma_{21} \rho_{22} - (i\Omega_p \rho_{12} + \text{c.c.}), \quad (\text{A1a})$$

$$\frac{\partial}{\partial t} \rho_{22} = \Gamma_{32} \rho_{33} - \Gamma_{21} \rho_{22} - (i\Omega_c \rho_{23} - i\Omega_p \rho_{12} + \text{c.c.}), \quad (\text{A1b})$$

$$\frac{\partial}{\partial t} \rho_{33} = -\Gamma_{32} \rho_{33} + (i\Omega_c \rho_{23} + \text{c.c.}), \quad (\text{A1c})$$

$$\frac{\partial}{\partial t} \rho_{32} = -g_{32} \rho_{32} + i\Omega_c \rho_{22} - i\Omega_c \rho_{33} - i\Omega_p^* \rho_{31} - iN_a \int d^3 r' V(\mathbf{r}' - \mathbf{r}) \rho_{33,32}(\mathbf{r}', \mathbf{r}, t). \quad (\text{A1d})$$

One can obtain dynamic equations for two-body density-matrix elements from above one-body equations, and then solve them using the perturbation method as explained in Sec. II. We are only interested in the third-order two-body density-matrix element  $\rho_{33,31}^{(3)}$  that determines the nonlocal nonlinear susceptibility  $\chi_R^{(3)}$ . It can be solved from the following equation:

$$Q \mathbf{x}^{(3)} = \mathbf{q}, \quad (\text{A2})$$

where  $\mathbf{x}^{(3)}(\mathbf{q})$  is a vector of the minimal number of third-order (two-order) two-body (two-body and one-body) density-matrix elements needed to get the desired solution, while  $Q$  denotes the corresponding coefficient matrix composed of some known parameters defined in Sec. II. To be more specific, we have

$$\mathbf{x}^{(3)} = [\rho_{22,21}^{(3)}, \rho_{22,31}^{(3)}, \rho_{33,21}^{(3)}, \rho_{33,31}^{(3)}, \rho_{32,21}^{(3)}, \rho_{21,23}^{(3)}, \rho_{32,31}^{(3)}, \rho_{31,23}^{(3)}]^T,$$

$$Q = \begin{bmatrix} M_{31} & \Omega_c^* & -i\Gamma_{23} & 0 & \Omega_c^* & -\Omega_c & 0 & 0 \\ \Omega_c & M_{32} & 0 & -i\Gamma_{23} & 0 & 0 & \Omega_c^* & -\Omega_c \\ 0 & 0 & M_{33} & \Omega_c^* & -\Omega_c^* & \Omega_c & 0 & 0 \\ 0 & 0 & \Omega_c & M_{34} & 0 & 0 & -\Omega_c^* & \Omega_c \\ \Omega_c & 0 & -\Omega_c & 0 & M_{35} & 0 & \Omega_c^* & 0 \\ -\Omega_c^* & 0 & \Omega_c^* & 0 & 0 & M_{36} & 0 & \Omega_c^* \\ 0 & \Omega_c & 0 & -\Omega_c & \Omega_c & 0 & M_{37} & 0 \\ 0 & -\Omega_c^* & 0 & \Omega_c^* & 0 & \Omega_c & 0 & M_{38} \end{bmatrix},$$

$$\mathbf{q} = \Omega_p [-\rho_{21,12}^{(2)} + \rho_{21,21}^{(2)} - \rho_{22}^{(2)}, -\rho_{31,12}^{(2)} + \rho_{21,31}^{(2)}, -\rho_{33}^{(2)}, 0, \rho_{21,31}^{(2)} - \rho_{32}^{(2)}, -\rho_{23}^{(2)} - \rho_{21,13}^{(2)}, \rho_{31,31}^{(2)}, -\rho_{31,13}^{(2)}]^T.$$

with  $M_{31} = i(g_{21} + \Gamma_{21})$ ,  $M_{32} = i(g_{31} + \Gamma_{32})$ ,  $M_{33} = i(g_{21} + \Gamma_{32})$ ,  $M_{34} = i(g_{21} + \Gamma_{32}) - V$ ,  $M_{35} = i(g_{21} + g_{32})$ ,  $M_{36} = i(g_{21} + g_{23})$ ,  $M_{37} = i(g_{31} + g_{32}) - V$ ,  $M_{38} = i(g_{23} + g_{31})$ , and  $\mathcal{P}_1 = g_{21}g_{31} + \Omega_c^2$ .

The second-order two-body density-matrix elements in  $\mathbf{q}$  obeys the following equations:

$$\begin{bmatrix} 2ig_{21} & 0 & 2\Omega_c^* \\ 0 & 2ig_{31} - V & 2\Omega_c \\ \Omega_c & \Omega_c^* & ig_{21} + ig_{31} \end{bmatrix} \begin{bmatrix} \rho_{21,21}^{(2)} \\ \rho_{31,31}^{(2)} \\ \rho_{31,21}^{(2)} \end{bmatrix} = -i \frac{|\Omega_p|^2}{\mathcal{P}_1^*} \begin{bmatrix} 2g_{31} \\ 0 \\ \Omega_c \end{bmatrix}, \quad (\text{A3})$$

$$\begin{bmatrix} 2iy_{21} & 0 & -\Omega_c & \Omega_c^* \\ 0 & 2iy_{31} & \Omega_c & -\Omega_c^* \\ -\Omega_c^* & \Omega_c^* & ig_{13} + ig_{21} & 0 \\ \Omega_c & -\Omega_c & 0 & ig_{12} + ig_{31} \end{bmatrix} \begin{bmatrix} \rho_{21,12}^{(2)} \\ \rho_{31,13}^{(2)} \\ \rho_{21,13}^{(2)} \\ \rho_{21,13}^{*(2)} \end{bmatrix} = \Omega_p^2 \begin{bmatrix} ig_{13}(\mathcal{P}_1^*)^{-1} - ig_{13}^* \mathcal{P}_1^{-1} \\ 0 \\ \Omega_c^*(\mathcal{P}_1^*)^{-1} \\ -\Omega_c \mathcal{P}_1^{-1} \end{bmatrix}.$$

At last, equations for relevant second-order one-body density-matrix elements are

$$\begin{bmatrix} -\Gamma_{21} & \Gamma_{32} & -i\Omega_c & i\Omega_c^* \\ 0 & -\Gamma_{32} & i\Omega_c & -i\Omega_c^* \\ i\Omega_c & -i\Omega_c & 0 & -g_{32} \\ -i\Omega_c^* & i\Omega_c^* & -g_{23} & 0 \end{bmatrix} \begin{bmatrix} \rho_{22}^{(2)} \\ \rho_{33}^{(2)} \\ \rho_{23}^{(2)} \\ \rho_{32}^{(2)} \end{bmatrix} = -\Omega_p^2 \begin{bmatrix} g_{31} \mathcal{P}_1^{-1} + g_{13}(\mathcal{P}_1^*)^{-1} \\ 0 \\ i\Omega_c \mathcal{P}_1^{-1} \\ -i\Omega_c(\mathcal{P}_1^*)^{-1} \end{bmatrix}. \quad (\text{A4})$$

- 
- [1] F. Goos and H. Hänchen, Ein neuer und fundamentaler versuch zur totalreflexion, *Ann. Phys. (Berlin, Ger.)* **436**, 333 (1947).
- [2] F. Goos and H. Lindberg-Hänchen, Neumessung des strahlversetzungseffektes bei totalreflexion, *Ann. Phys. (Berlin, Ger.)* **440**, 251 (1949).
- [3] K. Artmann, Berechnung der seitenversetzung des totalreflektierten strahles, *Ann. Phys. (Berlin, Ger.)* **437**, 87 (1948).
- [4] M. J. Adams, *An Introduction to Optical Waveguides* (Wiley-Interscience Publication, Wiley, New York, 1981), pp. 16–18.
- [5] M. A. Porras, Nonspecular reflection of general light beams at a dielectric interface, *Opt. Commun.* **135**, 369 (1997).
- [6] P. Balcou and L. Dutriaux, Dual Optical Tunneling Times in Frustrated Total Internal Reflection, *Phys. Rev. Lett.* **78**, 851 (1997).
- [7] A. Haibel, G. Nimtz, and A. A. Stahlhofen, Frustrated total reflection: The double-prism revisited, *Phys. Rev. E* **63**, 047601 (2001).
- [8] J. Stigloher, T. Taniguchi, H. S. Körner, M. Decker, T. Moriyama, T. Ono, and C. H. Back, Observation of a Goos-Hänchen-like Phase Shift for Magnetostatic Spin Waves, *Phys. Rev. Lett.* **121**, 137201 (2018).
- [9] V.-O. de Haan, J. Plomp, T. M. Rekveldt, W. H. Kraan, A. A. van Well, R. M. Dalgliesh, and S. Langridge, Observation of the Goos-Hänchen Shift with Neutrons, *Phys. Rev. Lett.* **104**, 010401 (2010).
- [10] Y. Liu, Z.-M. Yu, and S. A. Yang, Transverse shift in Andreev reflection, *Phys. Rev. B* **96**, 121101(R) (2017).
- [11] Z.-M. Yu, Y. Liu, Y. Yao, and S. A. Yang, Unconventional Pairing Induced Anomalous Transverse Shift in Andreev Reflection, *Phys. Rev. Lett.* **121**, 176602 (2018).
- [12] Y. Liu, Z.-M. Yu, C. Xiao, and S. A. Yang, Quantized Circulation of Anomalous Shift in Interface Reflection, *Phys. Rev. Lett.* **125**, 076801 (2020).
- [13] C.-F. Li, Negative Lateral Shift of a Light Beam Transmitted through a Dielectric Slab and Interaction of Boundary Effects, *Phys. Rev. Lett.* **91**, 133903 (2003).
- [14] H. M. Lai and S. W. Chan, Large and negative Goos-Hänchen shift near the Brewster dip on reflection from weakly absorbing media, *Opt. Lett.* **27**, 680 (2002).
- [15] L.-G. Wang, M. Ikram, and M. S. Zubairy, Control of the Goos-Hänchen shift of a light beam via a coherent driving field, *Phys. Rev. A* **77**, 023811 (2008).
- [16] H. R. Hamed, A. Radmehr, and M. Sahrai, Manipulation of Goos-Hänchen shifts in the atomic configuration of mercury via interacting dark-state resonances, *Phys. Rev. A* **90**, 053836 (2014).
- [17] T. Shui, W.-X. Yang, Q. Zhang, X. Liu, and L. Li, Squeezing-induced giant Goos-Hänchen shift and hypersensitized displacement sensor in a two-level atomic system, *Phys. Rev. A* **99**, 013806 (2019).
- [18] K. V. Sreekanth, Q. L. Ouyang, S. Han, K. T. Yong, and R. Singh, Giant enhancement in Goos-Hänchen shift at the singular phase of a nanophotonic cavity, *Appl. Phys. Lett.* **112**, 161109 (2018).
- [19] K. L. Tsakmakidis, A. D. Boardman, and O. Hess, ‘Trapped rainbow’ storage of light in metamaterials, *Nature (London)* **450**, 397 (2007).
- [20] R.-G. Wan and M. S. Zubairy, Coherent control of spatial and angular Goos-Hänchen shifts in a metal-clad waveguide structure, *Phys. Rev. A* **101**, 023837 (2020).
- [21] D. Felbacq and R. Smaïli, Bloch Modes Dressed by Evanescent Waves and the Generalized Goos-Hänchen Effect in Photonic Crystals, *Phys. Rev. Lett.* **92**, 193902 (2004).



- [22] H. Wu, Q. Luo, H. Chen, Y. Han, X. Yu, and S. Liu, Magnetically controllable nonreciprocal Goos-Hänchen shift supported by a magnetic plasmonic gradient metasurface, *Phys. Rev. A* **99**, 033820 (2019).
- [23] M. Ullah, A. Abbas, J. Jing, and L.-G. Wang, Flexible manipulation of the Goos-Hänchen shift in a cavity optomechanical system, *Phys. Rev. A* **100**, 063833 (2019).
- [24] G. Ye, W. Zhang, W. Wu, S. Chen, W. Shu, H. Luo, and S. Wen, Goos-Hänchen and Imbert-Fedorov effects in Weyl semimetals, *Phys. Rev. A* **99**, 023807 (2019).
- [25] L. G. Wang, H. Chen, and S. Y. Zhu, Large negative Goos-Hänchen shift from a weakly absorbing dielectric slab, *Opt. Lett.* **30**, 2936 (2005).
- [26] S. M. Anderson and B. S. Mendoza, Three-layer model for the surface second-harmonic generation yield including multiple reflections, *Phys. Rev. B* **94**, 115314 (2016).
- [27] V. J. Yallapragada, A. V. Gopal, and G. S. Agarwal, Goos-Hänchen shifts in harmonic generation from metals, *Opt. Express* **21**, 10878 (2013).
- [28] J. Sanchez-Curto, P. Chamorro-Posada, and G. S. McDonald, Giant Goos-Hänchen shifts and radiation-induced trapping of Helmholtz solitons at nonlinear interfaces, *Opt. Lett.* **36**, 3605 (2011).
- [29] P. Chamorro-Posada, J. Sanchez-Curto, A. B. Aceves, and G. S. McDonald, Widely varying giant Goos-Hänchen shifts from airy beams at nonlinear interfaces, *Opt. Lett.* **39**, 1378 (2014).
- [30] M. Fleischhauer, A. Imamoglu, and J. P. Marangos, Electromagnetically induced transparency: Optics in coherent media, *Rev. Mod. Phys.* **77**, 633 (2005).
- [31] H. Kang and Y. Zhu, Observation of Large Kerr Nonlinearity at Low Light Intensities, *Phys. Rev. Lett.* **91**, 093601 (2003).
- [32] S. E. Harris and L. V. Hau, Nonlinear Optics at Low Light Levels, *Phys. Rev. Lett.* **82**, 4611 (1999).
- [33] J. D. Pritchard, A. Gauguier, K. J. Weatherill, and C. S. Adams, Optical non-linearity in a dynamical Rydberg gas, *J. Phys. B: At., Mol. Opt. Phys.* **44**, 184019 (2011).
- [34] V. Parigi, E. Bimbard, J. Stanojevic, A. J. Hilliard, F. Nogrette, R. Tualle-Brouiri, A. Ourjoumtsev, and P. Grangier, Observation and Measurement of Interaction-Induced Dispersive Optical Nonlinearities in an Ensemble of Cold Rydberg Atoms, *Phys. Rev. Lett.* **109**, 233602 (2012).
- [35] A. Tebben, C. Hainaut, V. Walther, Y.-C. Zhang, G. Zürn, T. Pohl, and M. Weidemüller, Blockade-induced resonant enhancement of the optical nonlinearity in a Rydberg medium, *Phys. Rev. A* **100**, 063812 (2019).
- [36] S. Sevinçli, N. Henkel, C. Ates, and T. Pohl, Nonlocal Nonlinear Optics in Cold Rydberg Gases, *Phys. Rev. Lett.* **107**, 153001 (2011).
- [37] Z. Y. Bai and G. X. Huang, Enhanced third-order and fifth-order Kerr nonlinearities in a cold atomic system via Rydberg-Rydberg interaction, *Opt. Express* **24**, 4442 (2016).
- [38] Y. Mu, L. Qin, Z. Shi, and G. Huang, Giant Kerr nonlinearities and magneto-optical rotations in a Rydberg-atom gas via double electromagnetically induced transparency, *Phys. Rev. A* **103**, 043709 (2021).
- [39] S. Baur, D. Tiarks, G. Rempe, and S. Dürr, Single-Photon Switch Based on Rydberg Blockade, *Phys. Rev. Lett.* **112**, 073901 (2014).
- [40] H. Gorniaczyk, C. Tresp, J. Schmidt, H. Fedder, and S. Hofferberth, Single-Photon Transistor Mediated by Inter-state Rydberg Interactions, *Phys. Rev. Lett.* **113**, 053601 (2014).
- [41] A. V. Gorshkov, J. Otterbach, M. Fleischhauer, T. Pohl, and M. D. Lukin, Photon-Photon Interactions via Rydberg Blockade, *Phys. Rev. Lett.* **107**, 133602 (2011).
- [42] Z. Bai, W. Li, and G. Huang, Stable single light bullets and vortices and their active control in cold Rydberg gases, *Optica* **6**, 309 (2019).
- [43] D. H. Foster, A. K. Cook, and J. U. Nockel, Goos-Hänchen induced vector eigenmodes in a dome cavity, *Opt. Lett.* **32**, 1764 (2007).
- [44] M. Born and E. Wolf, *Principles of Optics*, 7th edition (Cambridge University Press, 1999).
- [45] T. F. Gallagher, *Rydberg Atoms* (Cambridge University Press, 2008).
- [46] J. D. Pritchard, D. Maxwell, A. Gauguier, K. J. Weatherill, M. P. A. Jones, and C. S. Adams, Cooperative Atom-Light Interaction in a Blocked Rydberg Ensemble, *Phys. Rev. Lett.* **105**, 193603 (2010).
- [47] M. Saffman, T. G. Walker, and K. Mølmer, Quantum information with Rydberg atoms, *Rev. Mod. Phys.* **82**, 2313 (2010).
- [48] Y. Wang, H. Li, Z. Cao, T. Yu, Q. Shen, and Y. He, Oscillating wave sensor based on the Goos-Hänchen effect, *Appl. Phys. Lett.* **92**, 061117 (2008).
- [49] T. Yu, H. Li, Z. Cao, Y. Wang, Q. Shen, and Y. He, Oscillating wave displacement sensor using the enhanced Goos-Hänchen effect in a symmetrical metal-cladding optical waveguide, *Opt. Lett.* **33**, 1001 (2008).
- [50] C.-W. Chen, W.-C. Lin, L.-S. Liao, Z.-H. Lin, H.-P. Chiang, P.-T. Leung, E. Sijercic, and W.-S. Tse, Optical temperature sensing based on the Goos-Hänchen effect, *Appl. Opt.* **46**, 5347 (2007).
- [51] X. Wang, M. Sang, W. Yuan, Y. Nie, and H. Luo, Optical relative humidity sensing based on oscillating wave-enhanced Goos-Hänchen shift, *IEEE Photonics Technol. Lett.* **28**, 264 (2016).
- [52] Y. S. Dadoenkova, F. F. L. Bentivegna, R. V. Petrov, and M. I. Bichurin, Principle of tunable chemical vapor detection exploiting the angular Goos-Hänchen shift in a magneto-electric liquid-crystal-based system, *J. Opt. (Bristol, UK)* **19**, 095802 (2017).
- [53] Ziauddin, S. Qamar, and M. S. Zubairy, Coherent control of the Goos-Hänchen shift, *Phys. Rev. A* **81**, 023821 (2010).
- [54] S. Liu, W.-X. Yang, and Z. Zhu, Coherent control of the Goos-Hänchen shift via Fano interference, *J. Appl. Phys.* **119**, 143101 (2016).